Eliminating Design Effort: A Reconfigurable Sensing Framework For Chipless, Backscatter Tags

Wenli Jiao[†‡], Ju Wang[†*], Yelu He[†], Xiangdong Xi[†],
Fuwei Wang[†‡], Dingyi Fang[†‡], Xiaojiang Chen[†‡*]
[†]Northwest University, China
[‡]Shaanxi International Joint Research Centre for the Battery-Free Internet of Things, China
{jiaowenli,202021316,way9890xxd}@stumail.nwu.edu.cn,{wangju,wfw,dyf,xjchen}@nwu.edu.cn

ABSTRACT

Backscatter tag based sensing has received a lot of attention recently due to the battery-free, low-cost and widespread use of backscatter tags, e.g., RFIDs. Despite that, they suffer from an extensive, costly, and time-consuming redesign effort when there are changes in application requirements, such as changes in sensing targets or working frequency bands.

This paper introduces a reconfigurable sensing framework, which enables us to easily reconfigure the design parameters of chipless backscatter tags for sensing different targets or working with different frequency bands, without the need of onerous design effort. To realize this vision, we capture the relationship between the application requirements and the sensing tag's design parameters. This relationship enables us to fast and efficiently reconfigure/change an existing sensing tag design for meeting new application requirements. Real-world experiments show that, by using our reconfigurable framework to flexibly redesign a tag's parameters, the sensing tag achieves more than 92.1% accuracy for sensing four different applications and working on four different frequency bands.

1 INTRODUCTION

Backscatter tag based sensing, which attaches a backscatter tag to a target and leverages distorted backscatter signals for sensing the target's attribute, has received a lot of attention recently due to the battery-free, low-cost and widespread use of backscatter tags, e.g., RFIDs. Many appealing applications are enabled by the backscatter tag based sensing, such as the material sensing [44], the soil moisture sensing [17, 25], the environment light intensity and temperature sensing [35, 39], the liquid identification [16, 18], the solid identification [18, 50], and the human input sensing [13].

Although existing backscatter tag based sensing systems achieved great success, they suffer from an extensive design effort which is costly and time-consuming. The reason is twofold. First, the design of a backscatter sensing tag requires not only expert experience on the microstrip circuit design, but also a long-time test process. Second, an existing designed sensing tag may only work on a specific application or a given frequency band. If the sensing application or the signal frequency band changes, one has to start from *zero* to redesign a new backscatter sensing tag to meet the new application requirement. For example, LiveTag [13] is a dedicated Wi-Fi backscatter tag designed for sensing discrete finger touch only. If one wants to use the LiveTag for other sensing applications (e.g., soil moisture sensing), one would need to completely redesign the tag from scratch, which however requires time-consuming simulation, fabrication and testing. For instance, most RFID-based backscatter sensing systems only work for a specific application and require careful tag selection, tag deployment, and feature extraction, e.g., GreenTag [41], which is a dedicated soil moisture sensing system and only works with RFID.

Ideally, we want a reconfigurable sensing system/framework that can support generalized sensing for different applications and different frequency bands. Many applications would benefit from generalized sensing. Specifically, one can simply reconfigure the design parameters of the tag designed for alcohol concentration sensing and then print the tag with new parameters for soil moisture sensing. Also, one can reconfigure design parameters of a tag that works in the Wi-Fi band to make it work with other IoT devices in a different frequency band, such as LoRA and RFID devices in 900 MHz, for outdoor, long-range sensing applications.

In this paper, we propose a reconfigurable sensing framework, which enables us to easily reconfigure the design parameters of chipless, backscatter tag for sensing different targets or working on different frequency bands, without the need for onerous design effort. Fig. 1 illustrates the overview and applications of the chipless backscatter tag based reconfigurable sensing framework. The Sensing Tag (i.e., S-Tag) is comprised of two antennas and a passive microstrip resonator circuit without any chip (i.e., chipless), and works with a pair of RF transceivers. The key sensing component of the S-Tag is a Defected Ground Structure (DGS) based resonator circuit [11], which is an etched slot on the metal ground. When an S-Tag is attached to a target, it takes the target as a part of the DGS resonator. Different targets' attributes make the DGS resonator produce different frequency responses, which in turn are utilized for identifying different target attributes, e.g., soil moisture levels. To illustrate this principle, Fig. 2(a) shows simulation results, where the two red lines represent two distinguishable frequency responses in the 2.4 GHz band (i.e., the gray area) for sensing two soil moisture levels.

To achieve generalized sensing, we aim to enable the sensing of a new target (e.g., the alcohol concentration) without changing RF transceivers since the replacement of them is costly for large-scale applications. The challenge, however, is that one cannot distinguish frequency response curves of the new target in the same frequency band without changing RF transceivers, e.g., the blue dotted lines as illustrated in Fig. 2(a). To solve the challenge, we aim to replace the sensing tag since the chipless and printable tags are low-cost and much cheaper than RF transceivers. Specifically, we reconfigure (i.e., change) the design parameters of the original sensing tag,

*Co-corresponding authors.

978-1-6654-9624-7/22/$31.00 ©2022 IEEE
DOI 10.1109/IPSN54338.2022.00032

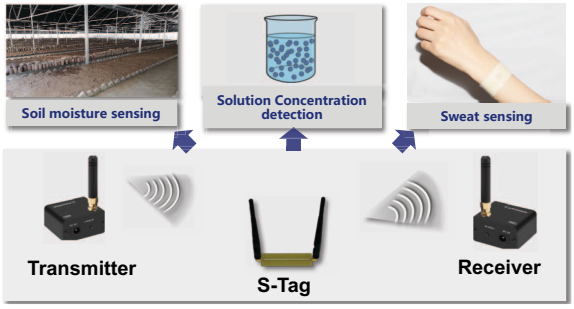

Figure 1: System overview and application examples of our backscatter tag based sensing framework.

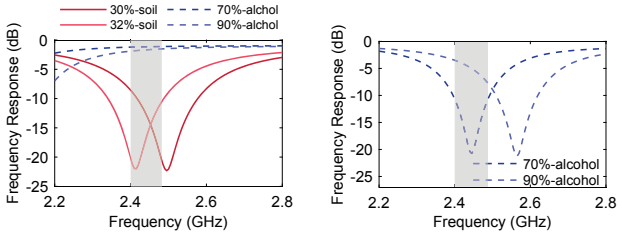

(a) In 2.4 GHz band, the S-Tag can sense soil moisture, but cannot sense alcohol concentration.

(b) The reconfigured S-Tag can sense alcohol concentration in 2.4 GHz band.

Figure 2: Illustration of "reconfigurable".

so that the frequency response curves of the new target will be distinguishable for identifying the alcohol concentration as shown in Fig. 2(b). To achieve this, the resonant frequency of the resonator should be changed, since frequency response values vary largely near the resonant frequency, which is helpful for sensing/detection. A simple method to change the resonant frequency is to change the DGS resonator's geometric size, since (i) the resonant frequency is determined by the DGS size, and (ii) the DGS is a fully passive printable circuit, making it easy to modify. To choose a proper DGS size, most existing methods [30, 47] exhaustively search for all possible size values, which not only is time-consuming and computation costly, but also requires expert experience on circuit design. Thus, existing methods are difficult to fast and cost-efficiently re-design a sensing tag that can satisfy a given working frequency band and sensing target.

To address the challenge, we introduce a reconfigurable tag design framework that takes the application requirements (i.e., the target permittivity and the working frequency band) as inputs, and calculates the optimal DGS size values quickly and efficiently for a new sensing application. To realize this vision, we build two relationship models to capture (i) the effect of different target permittivity values on the resonant frequency when the sensing target touches the DGS resonator, and (ii) the relationship between the equivalent circuit components and the DGS size. Given the sensing target and the frequency band, the first model can estimate equivalent circuit parameters of the DGS resonator. Then, the second model takes these equivalent circuit parameters as inputs and finds the optimal DGS size parameters. As a result, we can accelerate the design of the DGS resonator and make the tag's frequency response match with the new targets and the new frequency bands, avoiding a cumbersome and complicated redesign of the whole sensing tag.

Finally, we combat self-interference and multipath interference, which not only limit the tag's working range but also distort the tag's backscatter signal and result in a failure in communication and sensing. We employ beam-forming at the transceiver side to narrow down the radiation region to suppress self-interference and multipath interference. To do so, the transceivers first estimate the direction of the passive S-Tag and then align their beams with the S-Tag. As a result, it boosts the tag's backscatter signal and also reduces self-interference and multipath interference.

We built five prototypes of S-Tag to demonstrate the generalization ability of our framework in both the application dimension and the frequency dimension. For the application dimension, we show the sensing of four kinds of targets, i.e., soil moisture sensing, alcohol concentration detection, salt solution concentration detection, and sweat detection on skin. For the frequency dimension, we show the sensing in four frequency bands, i.e., 900 MHz, 2.4 GHz, 5.8 GHz and 2–5 GHz. We implement the S-Tag based sensing system with three types of devices, i.e., WARP radios, USRP radios and commercial Wi-Fi cards. Real-world experiments show that, by using the reconfigurable tag design framework and flexibly reconfiguring the size parameters of the S-Tag, we achieve more than 92.1% sensing accuracy for all four applications and all four frequency bands. Finally, we conduct an HFSS based simulation experiment to illustrate the effectiveness of our framework. The results show that the more complex the simulation task (e.g., more complex model, wider sweep range, more fine-grained search step), the more time our framework saves. Compared to the traditional HFSS search method, our framework achieves a time saving of 2∼3 orders of magnitude under three different search granularities, i.e., coarse granularity, medium granularity, and fine granularity.

This paper makes the following **contributions**:

- We introduce the first reconfigurable sensing framework, which enables us to easily reconfigure design parameters of chipless backscatter tags for different applications and frequency bands. This framework greatly reduces the design complexity and time consumption.
- We explore the relationship among the target attribute, resultant circuit parameters, and the resonant frequency, which is the basis of chipless, backscatter tag based sensing and can benefit the future sensing work.
- Comprehensive real-world experiments demonstrate the effectiveness of the proposed framework.

2 RELATED WORK

Our work is broadly related to two research areas: wireless sensing and chipless sensing.

2.1 Wireless Sensing

Wi-Fi-based Sensing. Wi-Fi sensing enables a large number of IoT applications, including location detection and target material sensing [17, 22, 27, 42]. The basic idea of Wi-Fi sensing can be divided into two types: penetrating-based sensing [17, 18] and reflection-based sensing [50]. Penetrating-based sensing proposal exploits the impact of the target material on the line-of-sight channel between the transmitter and the receiver. This sensing method

requires the size of the sensing target to be larger than the signal wavelength, in order to avoid signal diffraction on the surface of the object. If the sensing target is small, this sensing method will fail. This would limit the number of types that can be sensed. Compared to the Wi-Fi sensing, S-Tag detects the permittivity and conductivity of a sensing target, and is not limited by the target size. Therefore, S-Tag can enable a large number of sensing applications. Moreover, unlike the Wi-Fi sensing principles, S-Tag can be designed to transduce the impact of the target material on the wireless channel by reconfiguring the design parameters of S-Tag. The reflection-based sensing method [50] exploits the impact of target surface type/material on the Wi-Fi signal. This method can distinguish solid materials with different surface roughness but can not detect different materials with the same surface roughness such as different liquids. Different from the sensing principle, S-Tag identifies different target's property by attaching the sensing target on S-Tag's resonator component. The sensing target type of the S-Tag is complementary to that of this system.

Low-power backscatter sensing. The low power backscatter IoT sensor is comprised of three main components: the backscatter-based communication module (e.g., WiFi/LoRA backscatter [32, 51]), the micro-controller unit and the active sensor module. They are usually designed to achieve ultra low power in chips and communication modules, which, however, still relies on energy-harvesting [6]. Unfortunately, current energy harvesting efficiency [36, 52] can not support continuously sensing.

RFID-based sensing. RFID-based sensing [40, 43, 44] attracts a lot of attention due to the battery-free, low-cost and widely deployment of RFID tags. Existing RFID based sensing systems mainly focus on material sensing [49] and touch sensing [34]. Basically, they exploit the impact of the target on the impedance changes of RFID tag's antenna. However, changes on the tag's antenna impedance would degrade the tag's working range, which limits its real-world applications. RFID-tatoo [40] exploits the resonant frequency of the RFID antenna to detect the human speech information. Another work [19] senses moisture changes by adding a capacitor sensor to an RFID tag.

Different from RFID tags, the sensing structure of S-Tag does not affect its communication ability because S-Tag uses a dedicated resonator for sensing and retains the antenna for communication. In addition, redesigning RFID tags for different frequency bands may be another possible solution. However, the redesign involves hardware layout optimization and impedance matching problems, which are still costly, time-consuming and require expert experience. In contrast, our reconfigurable sensing framework makes the redesign of the S-Tag simple and fast.

2.2 Chipless Sensing

Chipless sensing has been proposed for sensing soil moisture [7, 19], air humidity [8, 31] or the liquid concentration [29, 46] by designing chipless UHF tag with special resonator circuit structure. For example, the work [7] explores the feasibility of using a monopole probe to sense soil moisture. A few literature [8, 31] leverages resonator-based chipless tag to sense air humidity. However, these approaches require an ultra-wide frequency band of about 1 GHz (e.g., 6–7 GHz). In addition, several literature [15, 21] leverage resonator-based chipless sensor to sense soil moisture. However, these systems require 670 MHz (i.e., 0.98–1.65 GHz) frequency band for sensing and rely on Radar devices or the vector network analyzers as readers [8, 31]. Unfortunately, current most of IoT devices has limited working frequency band and cannot support these chipless sensing proposals, thereby limiting their real-world applications. In addition to target sensing, chipless sensing has been used for sensing finger touch interactions via a pair of Wi-Fi devices [13]. This work can detect "touching" or "not touching" and does not focus on the target sensing.

In summary, existing chipless sensing tags lack generalization ability and are costly to be deployed in practice. In contrast, our S-Tag can be fast redesigned for different applications and different frequency bands by using the proposed reconfigurable design framework. Further, it can also reach a relatively long working range with the beam-forming function.

3 SYSTEM DESIGN

3.1 Sensing Principle

To enable S-Tag's sensing ability, the key design is the resonator circuit, i.e., a fully passive metal surface printed on a substrate. When a sensing target is attached to the resonator circuit, the target becomes a part of the circuit. Different target attributes (such as soil moisture levels, the salt solution concentration, the alcohol concentration and the human sweat on skin) will add different permittivity and/or conductivity values to the resonator circuit, resulting in changes of the S-Tag's frequency response. Thus, one can sense a target's attributes by using the frequency response feature. Next, we introduce S-Tag's structure and explain the sensing principle through equivalent circuit analysis.

Resonator. The resonator circuit can be realized by various geometrical structures such as the defected ground structure resonator [11], the microstrip ring resonators [12] and the spiral planar resonator [10]. We employ the square C-shaped DGS resonator as the passive sensor, since it is simple and easy to design. Compared to other shapes, the square C-shaped DGS has only two geometric parameters including its length and width. Fig. 3(a) shows the 3D structure of the DGS resonator. The transmission line is located in the middle of the top layer, and the square C-shaped DGS is located in the middle of the ground layer where the length a and the width w are two adjustable design parameters. Empirically, the DGS resonator is equivalent to a parallel resonant circuit (i.e., R_1, L_C, C_c) [47], as shown in Fig. 3(b). To sense the target, the DGS resonator acts as the sensing component, therefore the RLC circuit has a sensing port. According to the circuit theory [33], the frequency response can be computed as:

$$H(f) = |\frac{2Z_x}{-(2\pi f)^2 L^2 + j4\pi f L(1+Z_x) + 2Z_x + 1}|, \tag{1}$$

where, f is the signal frequency, L represents the inductance of the transmission line. Z_x represents the ground slot structure's impedance, which can be written as:

$$Z_x = \frac{1}{\frac{1}{R_1} + j2\pi f C_c + \frac{1}{j2\pi f L_c}} + \frac{1}{j2\pi f C_1}, \tag{2}$$

where R_1, L_C, C_c, are the equivalent resistor, inductor and capacitor of DGS resonator respectively. The transmission line, DGS and the ground plane form a capacitor C_1. When the imaginary part of the impedance Z_x in Eq. (2) achieves zero, the circuit achieves the

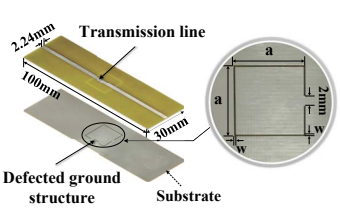

(a) The 3-D structure of the passive resonator.

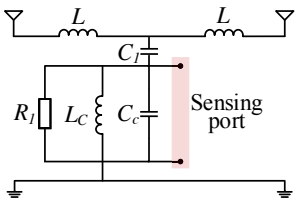

(b) The equivalent circuit of resonator.

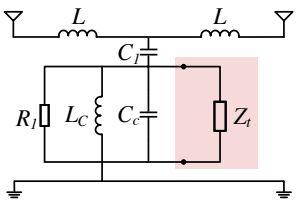

(c) The equivalent circuit of the resonator + target.

Figure 3: The resonator geometric structure and the its equivalent circuit.

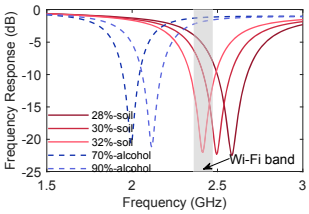

Figure 4: Frequency responses of different targets.

resonant state. Thus, the resonant frequency f_0 can be written as:

$$f_0 = \frac{1}{2\pi\sqrt{L_C(C_1 + C_c)}}. \tag{3}$$

Resonator + Target. When a sensing target contacts the DGS circuit, the target becomes a new circuit (its impedance denoted as Z_t [14]) and connects in parallel with the DGS circuit, as shown in Fig. 3(c). The impedance Z_t is related to the target permittivity ε [14]. We denote the impedance of the new DGS circuit as Z'_x. Thus, the frequency response of a target with permittivity ε is:

$$H'(f) = |\frac{2Z'_x}{-(2\pi f)^2 L^2 + j4\pi f L(1 + Z'_x) + 2Z'_x + 1}|, \tag{4}$$

where Z'_x can be computed as:

$$Z'_x = \frac{1}{\frac{1}{R_1} + \frac{1}{j2\pi f L_C} + j2\pi f C_c + \frac{1}{Z_t}} + \frac{1}{j2\pi f C_1}. \tag{5}$$

Now, the S-Tag has a new resonant frequency f'_0. Specifically, when the imaginary part of Z'_x is equal to zero, we can compute the new resonant frequency f'_0, which is the function of the circuit parameters (L_C, C_1, C_c, Z_t).

Conclusion: Different targets have different values for permittivity ε, resulting in different values for frequency response $H'(f)$. As a result, the frequency response $H'(f)$ can be used for target sensing. In theory, the phase of $H'(f)$ can also be used for target sensing. However, capturing the phase change requires precise synchronization of transceivers, which is not supported by most existing commercial RF devices (e.g., Wi-Fi, LoRA). In addition, the phase is susceptible to multipath interference, and it is difficult to remove the impact of multipath. Therefore, this paper exploits the amplitude of $H'(f)$ for sensing.

3.2 Reconfigurable Sensing

We show the motivation for reconfigurable sensing in Fig. 4. There is a sensing tag working with Wi-Fi transceivers in the 2.4 GHz Wi-Fi band for soil moisture sensing. When the sensing target changes from soil to alcohol solution, frequency response curves of alcohol solution (i.e., blue dotted lines) are very close to each other and hard to distinguish in the Wi-Fi band. Because Wi-Fi transceivers can only measure the frequency response within the Wi-Fi band, we aim to make the frequency response curves of alcohol solution distinguishable in the Wi-Fi band. To do so, the resonant frequency of the tag should be changed, since frequency response values vary largely near the resonant frequency, which is helpful for sensing/detection. A simple method to change the resonant frequency is to change the DGS size, since (i) the DGS's resonant frequency is determined by the DGS size, and (ii) the DGS is a fully passive printable circuit, which is easy to modify/change.

Now, the objective of reconfiguration is: *Given the working frequency band, and the target permittivity range,*[1] *we aim to quickly and efficiently find the best DGS size so that the frequency responses for the sensing target are distinguishable in the given frequency band.* Formally, the goal is making the frequency response $H'(f)$ in Eq. (4) of a target with permittivity range of $[\varepsilon_l,\ \varepsilon_h]$ distinguishable in the given band $[f_l,\ f_h]$. Specifically, note that the resonant frequency shifts to the left with the increasing of permittivity, so if the resonant frequency $f'_0(\varepsilon_l)$ of permittivity ε_l is slightly higher than f_h (i.e., $f'_0(\varepsilon_l) \geq f_h$) or the resonant frequency $f'_0(\varepsilon_h)$ of permittivity ε_h is slightly lower than f_l (i.e., $f'_0(\varepsilon_h) \leq f_l$), the frequency response of different permittivity in frequency range $[f_l,\ f_h]$ can be distinguishable.

To choose a proper DGS size (i.e., the length a and the width w), most existing methods [30, 47] calculate frequency responses exhaustively for all possible parameter combinations. However, this method is time-consuming and computation costly, i.e., requiring a significant design effort. Suppose that the length a has P values, the width w has Q values, and the time cost of each frequency response calculation of a parameter combination is T, where the average T is 2 mins[2]. Then, the computational complexity of searching all possible parameter combinations is $O(P \times Q \times T)$.

To determine the optimal DGS size quickly and effectively, we establish the relationship between the DGS size parameters and application requirements (e.g., frequency band and target permittivity range), one can therefore calculate the size parameters directly, avoiding the extensive search process. Next, we detail the relationship model.

3.2.1 Model the relationship between application requirements (e.g., target permittivity) and circuit parameters. In order to fast adjust the resonant frequency of DGS, we need to solve the new resonant frequency f'_0 by putting the concrete impedance Z_t of target into Z'_x of Eq. (5). However, the exact formula of f'_0 is highly complicated and thus it is hard to compute for a concrete expression of f'_0. To address this problem, we simplify the equivalent circuit of "Resonator + Target" (shown in Fig. 3(c)) by multiplying coefficient values and the target permittivity value by each circuit components L_c, C_1, C_c. Specifically, the new circuit parameters can be written

[1]The permittivity can be computed from existing functions between the target's attribute and its permittivity [38, 45, 48].

[2]We test the time cost of frequency response calculation of HFSS software using a PC with CPU of AMD Ryzen7 5800X 8-Core Processor and memory of 32 GB. The average T is 2 mins over 100 tests.

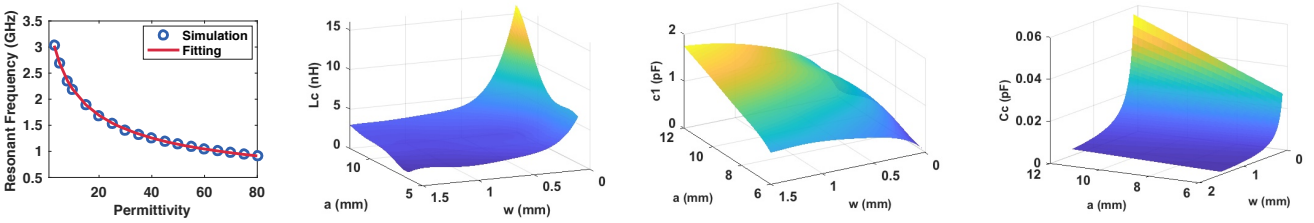

(a) Determine α, β, γ in Eq. (7). (b) L_C vs. <a, w>. (c) C_1 vs. <a, w>. (d) C_c vs. <a, w>.

Figure 5: (a) shows the relationship between the resonant frequency and the permittivity; (b), (c), and (d) show the relationship between the equivalent circuit parameters and the geometric size.

as:

$$\begin{aligned} L_c' &= L_c \cdot \alpha, \\ C_1' &= C_1 \cdot \varepsilon \cdot \beta, \\ C_c' &= C_c \cdot \varepsilon \cdot 1, \end{aligned} \tag{6}$$

where, α represents the effect of target on inductor, β represents the effect of target on the capacitor C_1, and ε is the target permittivity.

To determine the two coefficients α and β, our idea is fitting the frequency points over multiple permittivity values obtained from HFSS simulations. To do so, we formulate the new resonant frequency f_0' based on Eq. (6) as:

$$f_0' = \frac{1}{2\pi\sqrt{L_c \cdot \alpha \cdot (C_1 \cdot \varepsilon \cdot \beta + C_c \cdot \varepsilon + c_0 \cdot \varepsilon \cdot \gamma)}}. \tag{7}$$

where γ represents the plate area of the target's equivalent capacitor and $c_0 \cdot \varepsilon \cdot \gamma$ represents the equivalent capacitance formed by the target itself. Then, we can determine the coefficients α and β by fitting f_0' in Eq. (7) with simulated values. Fig. 5(a) gives an example of fitting Eq. (7) with the simulated resonant frequency points when permittivity changes. We can see that the red curve matches exactly with simulated values (i.e., the blue dots) and the goodness of fit R^2 is 0.9999. Then, we obtain the coefficients α=0.9∼1, β=0.05∼0.5, as well as γ=0.007∼0.01. This result verifies that the simplified approximation form (Eq. (6)) is good enough for calculating the resonant frequency and the equivalent circuit parameters.

Verification of the relationship model. Although the relationship shown in Eq. (6) comes from our intuitions, we further verify it through matching the simulated frequency response with the calculated frequency response from Eq. (4). Fig. 6 shows two frequency response curves: one is obtained from HFSS simulation and the other is calculated from Eq. (4). We can see that two curves match well with each other, indicating that the simplified circuit parameters are correct, i.e., the relationship model (6) is correct.

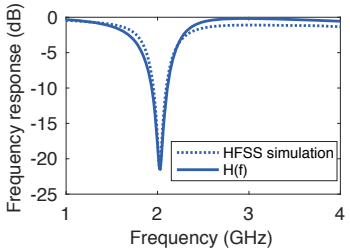

Figure 6: Verify the new circuit parameters in Eq. (6).

Find the circuit parameters. So far, we have built the relationship between the new resonant frequency f_0' and the circuit parameters. Now, we focus on how to compute the appropriate equivalent circuit parameters L_c, C_1, C_c, given the resonant frequency f_0' in $[f_l,\ f_h]$ and the target permittivity in $[\varepsilon_l,\ \varepsilon_h]$. To find $< L_c, C_1, C_c >$, we need to solve the two inequalities as:

$$\begin{aligned} \frac{1}{2\pi\sqrt{L_c \cdot \alpha \cdot (C_1 \cdot \varepsilon_l \cdot \beta + C_c \cdot \varepsilon_l + c_0 \cdot \varepsilon_l \cdot \gamma)}} &\geq f_h, \\ \frac{1}{2\pi\sqrt{L_c \cdot \alpha \cdot (C_1 \cdot \varepsilon_h \cdot \beta + C_c \cdot \varepsilon_h + c_0 \cdot \varepsilon_h \cdot \gamma)}} &\leq f_l. \end{aligned} \tag{8}$$

The above two inequalities can be solved by using the searching algorithm, such as the steepest gradient descent and Newton method. For example, given the target permittivity ε=5 and the working frequency band $f \in$[4.9, 5.8] GHz, we obtain the equivalent circuit parameter that can meet this requirement are L_c=0.56∼1.4 nH, C_1=0.1∼0.7 pF, C_c=0.001∼0.05 pF. Next, we show how to obtain the DGS size that can satisfy the three circuit parameters.

3.2.2 Model the relationship between circuit parameters and the DGS size. To determine the relationship between circuit parameters <L_c, C_1, C_c> and the DGS's length and width <a,w>, our basic idea is to match the frequency response from HFSS simulation and the calculated frequency response from Eq. (1). This task can be formulated as an optimization problem, i.e., finding the optimal circuit parameters <L_c, C_1, C_c> so that the difference between the calculated frequency response and HFSS simulation frequency response is minimized. We solve this optimization problem by using an improved differential evolution algorithm [37]. After obtaining these meta mapping dataset, we can model the relationship between each circuit parameter by fitting these meta mapping dataset. Fig. 5(b), 5(c) and 5(d) show the relationship between three circuit parameters L_c, C_1, C_c and the DGS size <a,w>. It is noted that our method is applicable to all C-shaped DGS structures. If we change the material and thickness of the substrate, we can still fast build this relationship. In Sec. 6, we discuss how to apply this method to different substrate materials and thicknesses, as well as other types of resonators.

Find the DGS size. Now, we can determine the DGS length and width based on Fig. 5(b), Fig. 5(c), Fig. 5(d) according to the circuit parameters obtained in the last subsection. Specifically, each circuit parameter corresponds to a surface that depicts the relationship between the parameter and the DGS size <a,w>, as well as two high and low boundaries that meet the frequency band criteria. In Fig. 7, the red and gray planes represent the low boundary and the high boundary respectively. A set of <a,w> corresponding to the range of the circuit parameter is formed by the projection area of the intersection area of the curved surface and the two planes on

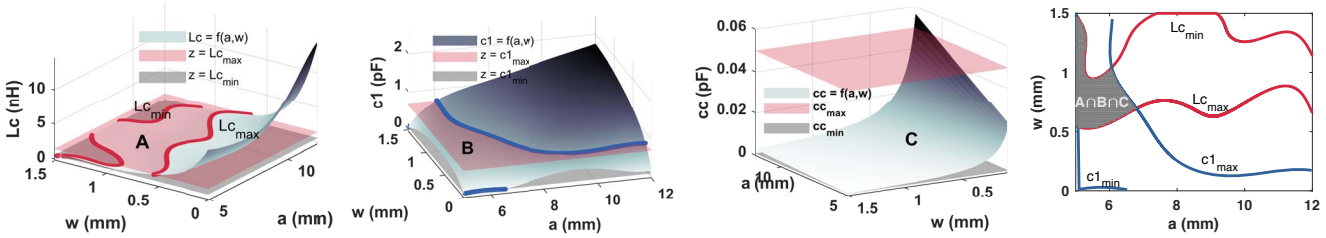

(a) $L_c = 0.56 \sim 1.37nH$. (b) $C_1 = 0.1 \sim 0.7pF$. (c) $C_c = 0.001 \sim 0.05pF$. (d) $Lc = 0.56 \sim 1.4nH$ and $C_1 = 0.1 \sim 0.7pF$ and $C_c = 0.001 \sim 0.05pF$.

Figure 7: An illustration example for finding the DGS size <a,w>.

the a-w plane. The three parameters correspond to three different point sets, and the intersection of the three point sets is the <a,w> set, which simultaneously meets the three circuit parameter ranges.

Fig. 7(a), 7(b), 7(c) show three <a, w> set – A, B, C corresponding to L_c=0.56~1.37 nH, C_1=0.1~0.7 pF, C_c=0.001~0.05 pF, respectively. Fig. 7(d) shows the final <a,w> set (i.e., $A \cap B \cap C$) that simultaneously meets the value range of three circuit parameters. We randomly pick three <a,w> parameters inside the gray area in Fig. 7(d) (i.e., <5.7, 1.34>,<5.3, 1>,<5.26, 1.09> (mm)) and verify its correctness through HFSS simulation. Results show that the resonant frequency of the three <a,w> combinations are 5.145 GHz, 5.1 GHz and 5.315 GHz, which satisfy the constraints of the frequency band $f \in$[4.9, 5.8] GHz.

3.3 Time Cost Analysis

So far, we have introduced how to build the reconfigurable tag design framework and how the framework works. Here, we analyze the time cost of using the reconfigurable framework to obtain a proper DGS size and that of using the HFSS based method under an ordinary computer hardware configuration[3]. The DGS resonator model used in this section is shown in Fig. 3(a).

- The main time cost of our framework comes from modeling the relationship between circuit parameters and the DGS size, which has two stages: (i) the time overhead $t1$ mins for obtaining the mapping dataset through HFSS simulation, (ii) the time overhead $t2$ mins for finding the circuit parameters and (iii) the time overhead T_3 of finding the DGS size.
- The traditional HFSS method calculates frequency responses exhaustively for all possible DGS size parameter combinations.
- In addition, HFSS based design method needs to simulate the model of "resonator + target", while our framework only needs to simulate the "resonator model" (without target) instead to obtain the meta-dataset.
- Suppose there are M targets, N frequency bands, the DGS length has P possible values, the DGS width has Q possible values.
- Denote the time consumption of the reconfigurable framework as T_{S-Tag}, we have $T_{S-Tag} = t1 + t2 + M \times N \times T3$, where $t1 = P \times Q \times T_1$, $t2 = P \times Q \times T_2$. T_1 is the time for simulating "resonator" (without target), which usually is about 1.5 minutes. T_2 is the time to calculate a set of circuit parameter values (i.e. L_C, C_1, C_c, R and L) based on the size of each set of DGS. T_2 and T_3 are usually less than 5 s.
- Denote the time consumption as T_{HFSS}. We have $T_{HFSS} = M \times N \times P \times Q \times T_4$. T_4 is the time for simulating "resonator + target", which usually is slightly more than 2 minutes.
- Thus, when M, N,P and Q are large in complex tasks, we have $T_{HFSS} \gg T_{S-Tag}$.

To better understand the inner operation, we show the computation process in brief. HFSS uses a numerical technique called the Finite Element Method (FEM), where a structure is subdivided into many smaller elements to calculate field solution [9]. Then, HFSS employs Finite Difference Time Domain (FDTD)[4] [23] to solve the electric field and magnetic field solutions for each element. To calculate an accurate solution, the two operations, i.e., meshing and solving Maxwell's equations, need multiple iterations. That is why the HFSS is time-consuming. For each DGS size setting, HFSS needs to perform the same iterative solution process. Although the time consumption is relative low (2~4 minutes) for one DGS size setting, the total calculation time increases dramatically when the number of DGS size settings increases. In contrast, our method transforms the two complicated operations into solving for the intersection of solutions of two inequalities, thereby reducing the complexity and time consumption.

Note that using a high-performance work station may greatly reduce the time cost of HFSS simulations. However, it will increase the hardware cost. Even if one uses the high-performance work station, the time consumed by our framework is still less than the HFSS based design method because the time for building our framework will also be reduced. As a summarize, our framework saves the time consumption for redesigning the S-Tag.

3.4 Combating Self-Interference and Multipath Interference

Self-interference and multipath reflection interference are two of the key challenges in backscatter communication and sensing [13, 51]. They not only limit a tag's working range but also distort the tag's backscatter signal, resulting in a failure in communication and sensing. To address the self-interference and multipath issue, our key idea is that: if the transmitter and the receiver can perform beam-forming and point their beams to the passive S-Tag, then it not only can reduce the self-interference and multipath interference,

[3]The PC has a CPU of AMD Ryzen7 5800X 8-Core Processor and memory of 32 GB.

[4]Finite Difference Time Domain is a state-of-the-art method for solving Maxwell's equations in complex geometries [20].

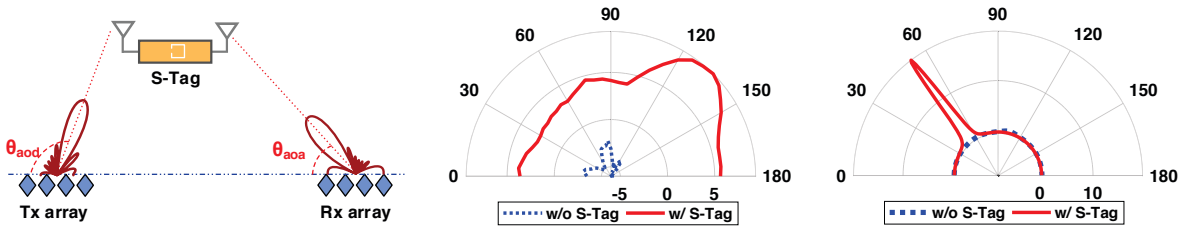

(a) Beam alignment method. (b) Power spectra of AoD profiles. (c) Power spectra of AoA profiles.

Figure 8: Estimate the direction of tag relative to the transmitter and receiver by comparing the power spectra profiles in two cases, i.e., without S-Tag and with S-Tag.

as shown in Fig. 8(a), but also can strengthen the incident signal to the tag and the backscattered signal from the tag, i.e., improving the tag's working range.

Conventional beam-forming relies on the receiver to feedback its channel state information (CSI) to the transmitter and then uses this CSI to precode the transmission to create beam-forming. The CSI is obtained by performing channel estimation of the receiver. However, it is impossible to perform channel estimations between S-Tag and transceivers, since the passive S-Tag has no battery.

To address this problem, instead of estimating CSI, we estimate the AoA (Angle of Arrival) and AoD (Angle of Departure) between the S-Tag and transceivers for beam-forming. Because if transceivers know the AoA and AoD, they can steer their beams to S-Tag directly without the need of CSI. To estimate the AoA and AoD, the key observation is that: when the transmitter's beam points at the tag, the power spectrum of AoD profile could have a peak. Similarly, if there is a signal arriving at the receiver, there is a peak in the power spectrum of AoA profile. To avoid the effect of multipath on power spectra of AoA and AoD, we find the true peaks corresponding to the S-Tag by comparing the two spectra with S-Tag and without S-Tag. As shown in Fig. 8(b) and 8(c), we can find that S-Tag is at $\theta_{aod} = 130°$ relative to the transmitter and at $\theta_{aod} = 55°$ relative to the receiver.

Specifically, to obtain the power spectrum of AoD profile, the transmitter steers its beam to scan the space while the receiver measures the power of received packets. At each angle, the receiver collects the data packets and calculates the corresponding power spectrum. To obtain the power spectrum of AoA profile, the receiver's antenna array obtain the phase of the received signal and compute the phase difference between antennas. Afterwards, we use MUSIC algorithm [26, 28] to obtain the power spectrum of AoA profile.

To illustrate this method, we conduct an experiment where the transmitter and the receiver are placed in a line with a separation of 4 m. The vertical distance between the S-Tag and this line is 2 m. The transmitter steers its beam from 0° to 180° at a step of 5°. For the AoA profile, the receiver performs MUSIC algorithm with an angle resolution of 1°. Following the procedure shown above, we can obtain the power spectra in two cases, i.e., without S-Tag and with S-Tag. Fig. 8(b) and Fig. 8(c) show the power spectra of AoA and AoD profiles respectively. It shows that S-Tag is at $\theta_{aod} = 130°$ relative to the transmitter and Fig. 8(c) shows that S-Tag is at $\theta_{aod} = 55°$ relative to the receiver. In Sec. 5.2.1, we evaluate the performance of the tag's angle estimation method.

In summary, when the transceivers align their beams with the S-Tag, multiple antennas in the transmitter and receiver can produce narrower beams, which can reduce the multipath interference from the surrounding objects and suppress the self-interference, and finally increase the working range.

3.5 Target Sensing

As illustrated in Sec. 3.1, we use the frequency response in a given band as the feature of a target's attribute, e.g., the liquid concentration and soil moisture. However, when S-Tag is deployed in different locations, the distance between transceivers and S-Tag will be different, resulting in variations in the frequency response. This variation breaks the one-to-one mapping between the target attribute and the frequency response feature, resulting in sensing errors. To cope with this problem, we borrow the idea in recent work [41] and use the ratio between a measured channel response and a reference channel response. The reference channel response is measured when the tag is shorted[5] Then, the channel response ratio is only related to a target's attribute and independent from the distance changes. In the following, the channel response ratio is called as the relative frequency response.

After obtaining the relative frequency response features of a target's attributes, we employ a machine learning based method to identify the target's attribute. First, we build a database which maps a target's attributes (i.e., the label termed as y) to the relative frequency response feature termed as vector $\mathbf{x}$, which forms the data sample $\{[x_1, x_2, ..., x_n], y\}$. To prevent the over-fitting, more training data samples are better for producing a more robust classifier. In this work, we collect 500 data samples for each property (e.g., the concentration level, the moisture level) for each sensing target. Second, we train the classifier (such as KNN) using the database and each type of sensing target has its own classifier using its corresponding dataset. Finally, we identify the target's attribute by inputting the measured relative frequency response feature of an unknown test target into the trained classifier.

4 IMPLEMENTATION

S-Tag fabrication. S-Tag is comprised of a microstrip resonator and two antenna as shown in Fig. 9(a). The first prototype is a simple version of S-Tag, which has a printed DGS resonator and two detachable antennas, shown in Fig. 9(a)-1. When a use case

[5]S-Tag is essentially a two-ports bandstop filter. The shorted S-Tag means that the signal passes through the S-Tag without attenuation.

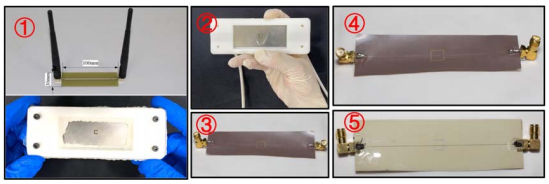

(a) The fabricated five S-Tag prototypes.

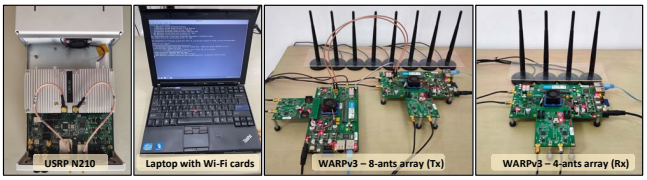

(b) Three kinds of transceivers.

Figure 9: The fabricated S-Tags (a), the transceivers (b).

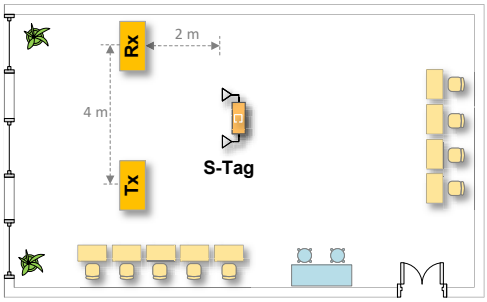

Figure 10: Deployment layout.

requires a longer sensing distance, one can employ antennas with higher gain. Below picture Fig. 9(a)-1, the S-Tag is encapsulated in a waterproof case, and only the DGS part is exposed for sensing the target. This design allows tag to be placed inside the target for sensing. Fig. 9(a)-2,3,4 show S-Tags that are used for sensing the solution concentration where the liquid is filled on the DGS structure. Additionally, we fabricated a S-Tag for skin sweat sensing, which has thee flexible substrate polydimethylsiloxane (abbr. PDMS [5]), shown in Fig. 9(a)-5. For the flexible S-Tag, the two conductive layers are made of conductive silver ink rather than copper. We use the micro-nano printer to print the transmission line and employ the squeegee technology to fabricate the 2D layout of DGS structure. One can print the antenna and resonator on the same PCB and stick S-Tag on the skin for easy use.

RF Transceivers. We test S-Tag with three types of RF transceivers including Atheros 9580 Wi-Fi cards, USRP radios [2] and WARP radios [3]. To test the sensing capability of S-Tag with commodity RF devices at 2.4 GHz and 5.8 GHz, we use two laptops with Atheros 9580 Wi-Fi cards as transceivers, where the PicoScenes software platform [24] is used to collect CSI readings as the frequency response. PicoScenes platform supports fine-grained CSI sampling across 56 subcarriers in each channel and also supports setting the transmitting and receiving power, which is easy to use. The three types of devices are shown in Fig. 9(b). To test the sensing capability of S-Tag at 900 MHz, we use two USRP N210 devices as transceivers. To evaluate the performance of S-Tag's angle estimation and the effect of beam-forming on the sensing accuracy, we use WARP radios as the transceiver. The transmitter is two cascaded WARP software radios configured with 8-antennas array. The receiver is one WARP board configured with 4-antennas array. All radios are connected to a PC via Ethernet cables for data collection. We implement data pre-process and identification algorithm in the PC. The code of beam scanning implementation is based on this work [1].

Experimental setup. Fig. 10 shows the default deployment layout, where the transmitter (Tx) and receiver (Rx) are placed with a space of 4 m, and both the Tx-tag distance and Rx-Tag distance are 2.8 m. In the experiment of evaluating the working range, we vary the distance between the transmitter and the tag. The experiments are conducted in an office room with a size of 7×10 m^2, furnished with several desks and chairs and some other furniture. For liquid sensing, we drop the liquid on the DGS structure of the tag, allowing the liquid to make full contact with the DGS resonator. For soil moisture sensing, we cover the soil completely with the S-Tag's DGS structure, so that the DGS is in contact with the soil. For sweat sensing, we stick the tag on the subject's forehead, so that the DGS is in full contact with the skin.

5 EXPERIMENT EVALUATION

In this section, we first conduct experiments to show the generalization of S-Tags in the frequency dimension and the application dimension in Sec. 5.1, followed by the discussion of the impact of system parameters in Sec. 5.2. Finally, we evaluate the time efficiency of the proposed reconfigurable framework in Sec. 5.3.

5.1 Generalization Ability

We verify the sensing function of S-Tag and demonstrate its generalization ability in frequency dimension and application dimension. We test four kinds of targets including NaCl solution, alcohol solution, soil moisture and sweat on skin.

- **NaCl solution**: The salt solution is a common liquid in our daily life such as the normal saline and the skin sweat. The attribute we detected is the conductivity. The conductivity is positively related to the salt concentration. In our experiment, the tested NaCl concentration are 0.1%, 0.5%, 1%, 6% and 10%.
- **Alcohol concentration**: Alcohol is another common and important liquid in medical and chemical fields. The detection of alcohol concentration is important for many applications. For example, 75% volume concentration alcohol is used in medical disinfection, and the industrial alcohol is 95% or 100%. In this experiment, the alcohol concentration are 70%, 80%, 90% and 100%.
- **Soil moisture**: Soil moisture detection plays an important role in the smart agriculture. A suitable moisture level not only improves plant productivity but also saves irrigation water [4]. In this experiment, the soil moisture levels are 5%, 10%, 15% and 20%.
- **Sweat on skin**: Monitoring the profile of metabolites in sweat plays an important role in medical care. Detecting

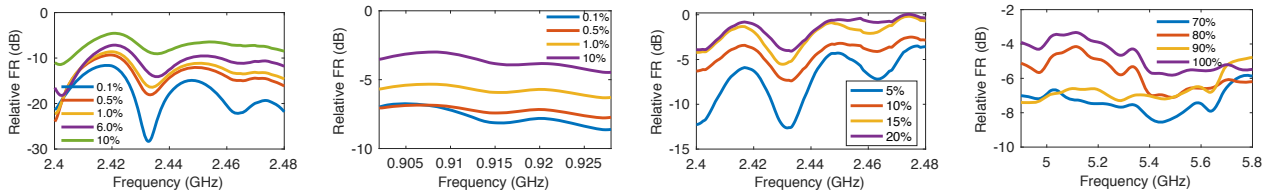

(a) NaCl concentration detection in 2.4 GHz with commodity Wi-Fi cards.
(b) NaCl concentration detection in 900 MHz with USRP radios.
(c) Soil moisture detection in 2.4 GHz with commodity Wi-Fi cards.
(d) Alcohol concentration detection in 5 GHz with commodity Wi-Fi cards.

Figure 11: The relative frequency response measured by USRP and Wi-Fi cards.

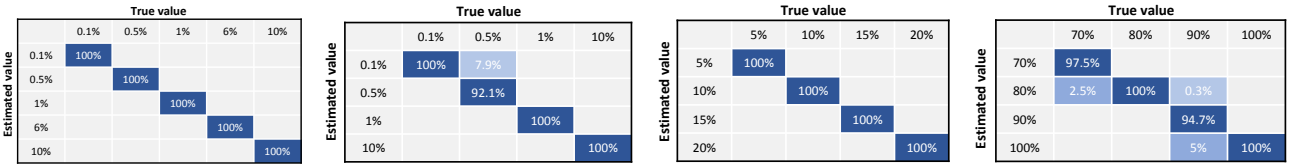

(a) NaCl sensing accuracy in 2.4 GHz.
(b) NaCl sensing accuracy in 900 MHz.
(c) Soil sensing accuracy in 2.4 GHz.
(d) Alcohol sensing accuracy in 5 GHz.

Figure 12: The sensing accuracy.

sweat can monitor human health without damaging human skin. In this experiment, we detect the sweat on skin under three movement states of a person.

Frequency bands: The test frequency bands are 900 MHz, 2.4 GHz, 5.8 GHz and 2–5 GHz. The combinations of application and frequency are shown in Table. 1.

Table 1: Generalization in frequency dimension and application dimension.

	900 MHz	2.4 GHz	5.8 GHz	2-5 GHz
NaCl concentration	✓	✓	–	–
Soil moisture	–	✓	–	–
Alcohol concentration	–	–	✓	–
Sweat on skin	–	–	–	✓

5.1.1 Generalization in frequency dimension. In reality, the user would choose the proper frequency band or RF devices depending on their application requirements or the availability of RF devices. For example, to achieve a long working range, the user may choose low frequency signals such as LoRA at 900 MHz. Also, if the Wi-Fi devices already exist in the user's environment, the user may choose the Wi-Fi signal. Thus, in this subsection, we evaluate the generalization ability in the frequency dimension. For NaCl solution, we first design a S-Tag that works with 2.4 GHz Wi-Fi as shown in Fig. 9(a)-3. Fig. 11(a) shows the relative frequency response feature measured by commercial Wi-Fi cards. We can see that these relative frequency response curves of the four concentration levels are distinguishable in the 2.4 GHz Wi-Fi band. With the concentration increasing, the amplitude of the frequency response curve gets higher, since the conductivity of solution rises as the concentration increasing. Fig. 12(a) shows that the detection accuracy of these concentration levels are 100%, demonstrating that the designed S-Tag works well for detecting NaCl solution concentration in 2.4 GHz band.

Then, we reconfigure this S-Tag to make it work in 900 MHz by modifying its DGS size as shown in Fig. 9(a)-4. Following the same experimental setting, we test its frequency response. Fig. 11(b) shows the relative frequency responses measured by USRP radios. These relative frequency response features are also distinguishable in 900 MHz and also show the same trend with the S-Tag in 2.4 GHz. Fig. 12(b) shows that the sensing accuracy is larger than 92% for detecting these concentration levels. This result verifies that the reconfigured S-Tag also works well in 900 MHz frequency band.

Conclusion: The two S-Tags and experimental results show that we can detect the concentration of salt solution in different bands by reconfiguring the size of DGS. In other words, it demonstrates the generalization capability of S-Tag in the frequency dimension.

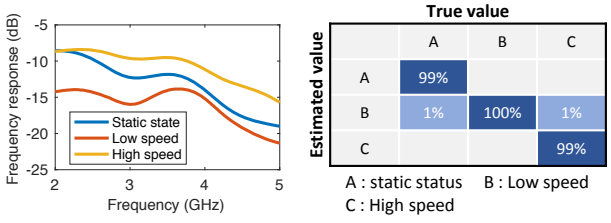

(a) Frequency response of the human head skin under three movement states.
(b) Skin sweat sensing accuracy.

Figure 13: A flexible S-Tag for sensing sweat on human skin.

5.1.2 Generalization in application dimension. To show the generalization ability in the application dimension, we show more applications, i.e., soil moisture sensing, alcohol concentration sensing and detection of sweat on skin.

Soil moisture sensing. To enable this application, we design a S-Tag for sensing soil moisture as shown in Fig. 9(a)-1. Fig. 11(c) shows the relative frequency response curves of four soil moisture levels measured by commercial Wi-Fi card. They are distinguishable in 2.4 GHz Wi-Fi band. As the soil moisture increasing, the relative frequency responses get higher. Fig. 12(c) shows that the sensing accuracy are 100% for these concentration levels, demonstrating the effectiveness of the S-Tag on detecting soil moisture level.

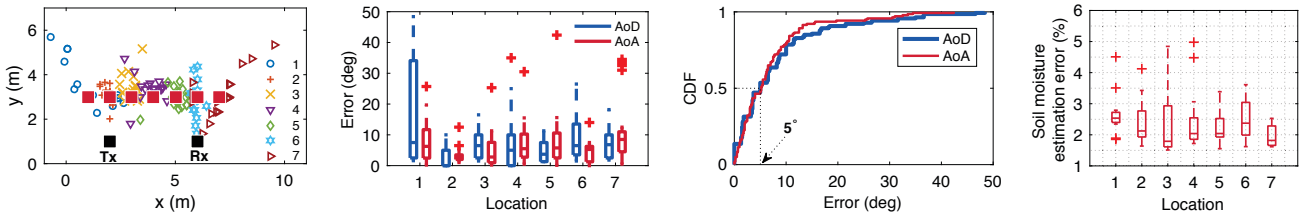

(a) Tag's location estimation results of 7 locations.

(b) Box plots of AoD and AoA estimation errors of 7 locations.

(c) CDF plots of the overall angle estimation errors.

(d) Soil moisture estimation error of 7 locations.

Figure 14: S-Tag's angle estimation results. The median AoD and AoA estimation error are 5° respectively.

Alcohol concentration sensing. To show a case study of alcohol concentration detection, we reconfigure the S-Tag in soil moisture sensing application to make it work in 5.8 GHz Wi-Fi band, which is shown in Fig. 9(a)-2. The tested alcohol are 70%–100% with a step of 10%. Fig. 11(d) shows the relative frequency response of different alcohol concentrations measured by WARP radios. Fig. 12(d) shows the sensing accuracy of the four levels are 97.5%, 100%, 94.7% and 100% respectively. This result also verifies the effectiveness of reconfigured S-Tag on detecting the alcohol concentration.

Detection of sweat on skin. To enable healthy related applications, the S-Tag should be flexible that can be attached on skin. Motivated by this requirement, we design a flexible S-Tag using PDMS material which is shown in Fig. 9(a)-5. The thickness of PDMS is 500 μm, which can be attached on skin.

To show the effectiveness of this S-Tag, we conduct an experiment to detect the sweat on the skin of a person to monitor the person's exercise status (such as judging whether there is excessive exercise). We asked three volunteers to run around the playground with low speed and high speed respectively and measured the frequency response of their skin after they stay static, run with low speed and high speed respectively. Fig. 13(a) shows the frequency response of one volunteer under three states. We can see that the three states produce three different frequency response features. We can distinguish the three state in 2–5 GHz band and achieve 99% sensing accuracy, which demonstrates the effectiveness of this S-Tag on the skin sweat sensing. This result also implies that this S-Tag can work with UWB devices.

Conclusion: The three S-Tags and experimental results show that we can enable different sensing applications by using the reconfigurable tag design framework to modify the size of DGS, demonstrating the generalization capability of S-Tag in the application dimension.

5.2 Impact of System Parameters

In this section, we first evaluate the performance of the proposed tag's angle estimation method. Then we evaluate the impact of beamforming parameter on the sensing result (the working range and the sensing error). The sensing target of this experiment is the soil moisture. The S-Tag is configured with two high gain antenna (about 16 dBi). The experiments are conducted under normal room temperature 25°C and ~50% air humidity. Note that, environmental factors (e.g., temperature and humidity) have very little influence on the sensing result since these factors have very little effect on the dielectric constant of air (ε_{air} = 1~1.001), which is not enough to significantly change the frequency response of the S-Tag.

5.2.1 The performance of tag's angle estimation. As illustrated in Sec. 3.4, the transceivers first estimate the tag's relative angle to them before beamforming. The performance of tag's angle estimation determines whether the transmitter and receiver can align beams with the tag, and also affects the sensing accuracy. To evaluate the performance of angle estimation, we place one S-Tag at 7 locations respectively and use the proposed angle estimation method to estimate the tag's angle. Both the Tx-Tag and Rx-Tag distance range from 2 m to 5.38 m. At each location, we perform angle estimation 20 times.

Fig. 14(a) shows the true locations 1~7 marked as the red squares from left to right. The Tx and Rx are marked as black squares. The estimated locations are marked as different types of symbols. We can see that most of the estimated locations are around their true locations. When the S-Tag is placed at the leftmost (Loc 1) and rightmost position (Loc 7), the number of estimated position points deviating from the true position are more than other locations. As shown in Fig. 14(b), the maximum AoD estimation error of Loc 1 is up to 48°, much higher than that of other locations. Similarly, the maximum AoA estimation error of Loc 7 is up to 35°, much higher than that of other locations. The large angle estimation errors result in these outliers. Overall, the angle estimation results for Loc 2, 4, and 5 are better than other locations. We further examine the overall performance of angle estimation. The CDF plot of the estimation error is shown in Fig. 14(c). The median estimation error of AoD and AoA are 5° respectively. The 90th percentile estimation errors of AoD and AoA are 18.4° and 13.2° respectively.

The impact of tag's deployment location on the sensing error. To examine the impact of tag's location on the sensing error, we compute the average frequency response of the S-Tag, and convert it to the sensing error. The experiment deployment is the same as Fig. 14(a). The sensing error at 7 locations are shown in Fig. 14(d). We find that the sensing error results are not well matched with the angle estimation error results. The possible reason is the side lobe leakage from the transmitter to the receiver. As the transmitter steers beam from 0° to 180°, the side lobe at the receiver's direction varies. The side lobe signal and the S-Tag's reflection signal superposition at the receiver, resulting in different frequency responses of S-Tag and slightly different sensing errors. The 10th~90th percentile sensing errors are in 1.5%~3%. This result indicates that the S-Tag should be deployed at the locations between

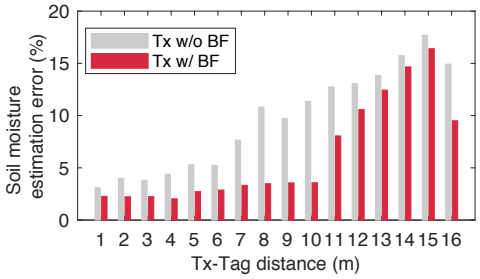

Figure 15: The effect of beam forming on improving the working range.

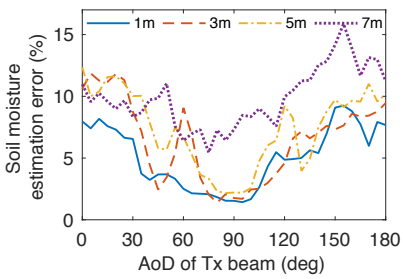

Figure 16: The impact of the angle of Tx beamforming on the sensing error.

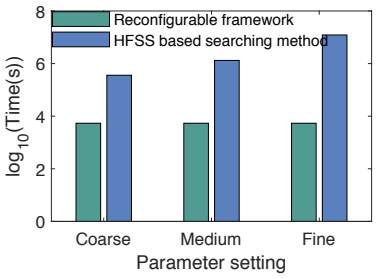

Figure 17: The time consumption comparison.

Loc 2 and Loc 6 to ensure accurate beam alignment and lower sensing error.

5.2.2 Tx beam-forming. Here, we evaluate the effect of beamforming on the working range and the impact of the angle of beamforming on the sensing error.

The effect of Tx beamforming on the working range. In this experiment, the deployment layout is the same as the previous experiment. We vary the Tx-Tag distance from 1 m to 16 m at a step size of 1 m. Fig. 15 reports the measurement results about how the sensing error varies with Tx-Tag distance. The gray bars represent the result without Tx beamforming while the red bars represent the result with Tx beamforming. We can see that in the case of without beamforming, the working range that the sensing error keeps lower than 5% is 4 m. In contrast, in the case of using beamforming, the working range can reach 10 m, an improvement of 1.5×. In addition, we find that the sensing error increases with the increasing of Tx-Tag distance. It is noted that the increase in sensing error is not related to the ratio method proposed in Sec. 3.5. The reason is the presence of the inevitable signal leakage from transmitter's side lobes to the receiver. With the distance increasing, the tag's signal gets weaker and is gradually masked by the side lobe leakage. Despite that, the distance gain of using beamforming technique is still high.

The impact of angle deviations of Tx beamforming on the sensing error. In practice, the transmitter's main beam lobe may not exactly point to the S-Tag's antenna due to the tag's angle estimation error and hardware imperfection. Therefore, we evaluate the impact of beam's angle deviation on the sensing error. In this experiment, one of the tag's antenna is placed in front of the transmitter's antenna array (90° direction) and the other is placed in front of the receiver's antenna array (90° direction). The Tx-Tag and Rx-Tag distance are fixed as 2 m and 0.5 m respectively. Fig. 16 reports the sensing error when the Tx beam changes the direction from 0° to 180°. We can see that the sensing error is lowest when the beam points to 90° direction, i.e., beam alignment. As the beam gradually deviating from the direction of tag, the sensing error increases. We find that a beam deviation of 6° (from 90° to 84°) results in an increase in the sensing error of ≈ 1% (from 2.967% to 3.804%). This indicates that the angle estimation accuracy should be as high as possible in order to improve the sensing accuracy.

5.3 Efficiency of Reconfigurable Framework

To evaluate the efficiency of the proposed reconfigurable framework, we compare it with traditional HFSS based parameter searching method. Specifically, we count the time consumed by the two methods to perform the same task. The task is to find the optimal DGS size, so that the target's resonant frequency is in 2.4~2.48 GHz. In this experiment, we adjust the length and width of DGS since the two parameters are the main factors related to the S-Tag's resonant frequency.

HFSS setting. The substrate of the DGS model is FR4 and the thickness is 1.2 mm. The length range of DGS is 5~12 mm, and the width range of DGS is 0.1~1.5 mm. In HFSS simulation setting, we set three kinds of DGS size parameter searching granularity, i.e., the coarse-grained, medium-grained and fine-grained, corresponding to the large, medium and small step size. For the length parameter, we set the three step sizes as 1 mm, 0.5 mm and 0.1 mm respectively. For the width parameter, we set the three step sizes as 0.4 mm, 0.2 mm and 0.1 mm respectively. In traditional HFSS based method, we optimize the length and width simultaneously and count the running time of each step setting. In the reconfigurable framework, we count both the time for the reconfigurable framework construction and the time for calculating DGS size. The number of the target permittivity are 100 (i.e., $M = 100$). The frequency sweeping range is 1~10 GHz at a step size of 0.01 GHz. Recall the time cost analysis in Sec. 3.3, where $T_{S-Tag} = PQT_1 + PQT_2 + MNT_3$, $T_{HFSS} = MNPQT_4$. In HFSS setting, the granularity corresponds to the value of P, Q. The value of P is the ratio between the size range and the step size. Thus, the finer granularity (i.e., smaller step size) means larger values of P and Q. In addition, the number of frequency band is 1, i.e., $N = 1$. In this experiment, we count the time for simulating the three granularities in case of one permittivity, and calculate the total time consumption of 100 permittivity values by multiplying the time with 100.

Results. Fig. 17 reports the time consumption comparison of our reconfiguration framework and HFSS based searching method. To better understand the magnitude difference of time consumption, we plot $\log_{10}(Time)$ where the unit of $Time$ is second. We can see that, as the step size becomes smaller, the time consumption of HFSS based searching method (the blue bars) increases by a factor of 10 while our method remains almost unchanged. This is because the reconfigurable framework does not need to perform repeated simulation operations and the time for calculating DGS size is extremely short (less than 2 s) which is almost negligible compared

to the HFSS based searching method. Overall, our method reduces the time consumption by 99.95%, 99.6% and 98.5% in fine-grained, medium-grained and coarse-grained setting respectively compared to HFSS based searching method. As a summarize, the proposed reconfigurable design framework can effectively shorten the design cycle and reduce the labor cost.

6 DISCUSSION

- **Push the circuit design framework to different substrate materials and thickness.** The substrate material, thickness and DGS size together determine the values of equivalent circuit parameters and the values of α, β, γ in the approximation models of Eq. (6) (7). Yet, the substrate material and thickness do not influence the equivalent circuit structure. If the material or thickness are changed, we only need to reset the substrate parameters (e.g., permittivity, loss tangent, density and thickness) and rebuild the second model (i.e., the mapping relationship between the DGS size and the equivalent circuit parameters), which is fast and only need to be done once. In fact, the changing space of the two variants is relatively small as the choice of substrate usually depends on the material cost or the application requirement (i.e., rigid or flexible substrate). In practical fabrication, the user should design the thickness of substrate depending on the manufacturer's material thickness specification. Therefore, in current reconfigurable tag design framework, the substrate's material and thickness are set as two given parameters.
- **Push the reconfigurable tag design framework to other chipless resonator forms.** In addition, one may wonder if the reconfigurable tag design framework can be used for designing other resonators such as the spiral resonator. The proposed reconfigurable sensing framework can also be applied to other resonator forms. Actually, the design flow is the same as the current DGS resonator based S-Tag design flow. To generalize to other resonators, the key is to modify the equivalent circuit approximation model in Eq. (6). Based on the DGS resonator's approximation model in Eq. (6), one may formulate a similar approximation model for another resonator. Other steps are the same as the process shown in Sec. 3.2. Therefore, our basic idea can be extended to other resonators based sensing tag design.
- **Push the working range.** The basic version of S-Tag shown in Fig. 9(a) has limited working range. In order to increase the working range, S-Tag can be configured with high gain antennas as illustrated in Sec. 5.2.2. Also, the antenna can be designed as the patch array antenna and be printed in the same substrate with the resonator.

7 CONCLUSION

This paper presented a reconfigurable sensing framework, which enables us to easily reconfigure the design parameters of chipless, backscatter tags for generalizing to different targets or different frequency bands. We achieve this by capturing the relationship between the application requirements and the sensing tag's design parameters. By utilizing this relationship, one can fast reconfigure a new sensing tag, avoiding exhaustively parameter search. Real-world experiments have demonstrated the effectiveness of the reconfigurable tag design framework on reducing the design time, and verified its generalization ability in both the frequency dimension and the application dimension. Finally, simulation results shows that our framework achieves the time saving of 2∼3 orders of magnitude compared to the traditional HFSS based parameter searching method, which means that our framework improves the design efficiency at least 100 times, and even more in complex task. We believe the proposed reconfigurable design framework would benefit other backscatter based sensing work.

ACKNOWLEDGMENTS

We thank Dr. Yuhui Ren for his help in the early research of this work. We also thank Dr. Zhiping Jiang for providing the PicoScenes platform and his help during the experiment stage. We also thank our reviewers and shepherd for their insightful feedback which helped improve this paper. This work is supported by the National Natural Science Foundation of China (61772422, 61972316), the NSFC A3 Foresight Program Grant 62061146001, the NSFC Youth Foundation (62002291). This work is also supported by the Shaanxi International Science and Technology Cooperation Program (2019KWZ-05, 2020KWZ-013), and the ShaanXi Science and Technology Innovation Team Support Project 2018TD-026.

REFERENCES

[1] A multi-user mimo ofdm library (in matlab) for the warp software radio, 2015. http://xyzhang.ucsd.edu/SDM/index.html.
[2] Usrp n210, 2015. https://www.ettus.com/all-products/un210-kit/.
[3] Warp project, 2015. http://warpproject.org/trac.
[4] Precision farming, 2020. https://www.scientificamerican.com/article/precision-farming/.
[5] Polydimethylsiloxane, 2021. https://en.wikipedia.org/wiki/Polydimethylsiloxane.
[6] Ali Abedi, Farzan Dehbashi, Mohammad Hossein Mazaheri, Omid Abari, and Tim Brecht. Witag: Seamless wifi backscatter communication. In *SIGCOMM*, pages 240–252, 2020.
[7] Daniel Alonso, Qianyun Zhang, Yue Gao, and Daniel Valderas. Uhf passive rfid-based sensor-less system to detect humidity for irrigation monitoring. *MICROW OPT TECHN LET*, 59(7):1709–1715, 2017.
[8] Emran Md. Amin, Md. Shakil Bhuiyan, Nemai C. Karmakar, and Bjorn Winther-Jensen. Development of a low cost printable chipless rfid humidity sensor. *IEEE Sensors Journal*, 14(1):140–149, 2014.
[9] Inc ANSYS. An introduction to hfss: Fundamental principles, concepts, and use. 2013.
[10] Guillaume Bailly, Amal Harrabi, Jrme Rossignol, Morgane Michel, Didier Stuerga, and Pribetich. Microstrip spiral resonator for microwave-based gas sensing. *IEEE Sensors Letters*, 1(4):1–4, 2017.
[11] A. Balalem, A. R. Ali, J. Machac, and A. Omar. Compact band-stop filter using an interdigital dgs structure. In *2008 14th Conference on Microwave Techniques*, pages 1–3, 2008.
[12] A Bogner, C Steiner, S Walter, J Kita, G Hagen, and R Moos. Planar microstrip ring resonators for microwave-based gas sensing: Design aspects and initial transducers for humidity and ammonia sensing. *Sensors*, 17(10):1–4, 2017.
[13] Xinyu Zhang Chuhan Gao, Yilong Li. Livetag: Sensing human-object interaction through passive chipless wifi tags. In *NSDI*, pages 533–546, April 2018.
[14] Kenneth S Cole and Robert H Cole. Dispersion and absorption in dielectrics i. alternating current characteristics. *The Journal of chemical physics*, 9(4):341–351, 1941.
[15] Shuvashis Dey, Prasanna Kalansuriya, and Nemai Chandra Karmakar. A novel time domain reflectometry based chipless rfid soil moisture sensor. In *2015 IEEE MTT-S International Microwave Symposium*, pages 1–4. IEEE, 2015.
[16] Ashutosh Dhekne, Mahanth Gowda, Yixuan Zhao, Haitham Hassanieh, and Romit Roy Choudhury. Liquid: A wireless liquid identifier. In *MobiSys*, pages 442–454, 2018.
[17] Jian Ding and Ranveer Chandra. Towards low cost soil sensing using wi-fi. In *MobiCom*, October 2019.
[18] Chao Feng, Jie Xiong, Liqiong Chang, Ju Wang, Xiaojiang Chen, Dingyi Fang, and Zhanyong Tang. Wimi: Target material identification with commodity wi-fi devices. In *ICDCS*, pages 700–710. IEEE, 2019.

[19] Newton S. S. M. Da Fonseca, Raimundo C. S. Freire, Adriano Batista, Glauco Fontgalland, and Smail Tedjini. A passive capacitive soil moisture and environment temperature uhf rfid based sensor for low cost agricultural applications. In *IMOC*, 2017.

[20] Stephen D Gedney. Introduction to the finite-difference time-domain (fdtd) method for electromagnetics. *Synthesis Lectures on Computational Electromagnetics*, 6(1):1–250, 2011.

[21] Sarath Gopalakrishnan, Jose Waimin, Nithin Raghunathan, Saurabh Bagchi, Ali Shakouri, and Rahim Rahimi. Battery-less wireless chipless sensor tag for subsoil moisture monitoring. *IEEE Sensors Journal*, 21(5):6071–6082, 2020.

[22] Peter Hillyard, Anh Luong, Alemayehu Solomon Abrar, Neal Patwari, Krishna Sundar, Robert Farney, Jason Burch, Christina Porucznik, and Sarah Hatch Pollard. Experience: Cross-technology radio respiratory monitoring performance study. In *MobiCom*, pages 487–496, 2018.

[23] Lumerical Inc. Finite difference time domain (fdtd) solver introduction, 2021. https://support.lumerical.com/hc/en-us/articles/360034914633-FDTD-solver.

[24] Zhiping Jiang. Picoscenes : Csi collection platform, 2021. https://ps.zpj.io/.

[25] Wenli Jiao, Ju Wang, Yelu He, Xiangdong Xi, and Xiaojiang Chen. Detecting soil moisture levels using battery-free wi-fi tag. *arXiv preprint arXiv:2202.03275*, 2022.

[26] Revati Joshi and Ashwinikumar Dhande. Direction of arrival estimation using music algorithm. *IJRET*, 3(3):633–636, 2014.

[27] Manikanta Kotaru, Kiran Joshi, Dinesh Bharadia, and Sachin Katti. Spotfi: Decimeter level localization using wifi. In *SIGCOMM*, pages 269–282, 2015.

[28] P Laxmikanth, S Susruthababu, L Surendra, S Suparshya Babu, and D Venkata Ratnam. Enhancing the performance of aoa estimation in wireless communication using the music algorithm. In *SPACES*, pages 448–452. IEEE, 2015.

[29] Zonghao Li and Sharmistha Bhadra. A flexible printed chipless rfid tag for concentration measurements of liquid solutions. In *2019 IEEE SENSORS*, pages 1–4. IEEE, 2019.

[30] Vidyadhar S Melkeri, SL Mallikarjun, and PV Hunagund. H-shape defected ground structure (dgs) embedded square patch antenna. *Journal Impact Factor*, 6(1):73–79, 2015.

[31] Raji Sasidharan Nair, Etienne Perret, Smail Tedjini, and Thierry Baron. A group-delay-based chipless rfid humidity tag sensor using silicon nanowires. *IEEE Antennas & Wireless Propagation Letters*, 12:729–732, 2013.

[32] Yao Peng, Longfei Shangguan, Yue Hu, Yujie Qian, Xianshang Lin, Xiaojiang Chen, Dingyi Fang, and Kyle Jamieson. Plora: A passive long-range data network from ambient lora transmissions. In *SIGCOMM*, pages 147–160, 2018.

[33] David M Pozar. *Microwave engineering*. John wiley & sons, 2011.

[34] Swadhin Pradhan, Eugene Chai, Karthikeyan Sundaresan, Lili Qiu, Mohammad A Khojastepour, and Sampath Rangarajan. Rio: A pervasive rfid-based touch gesture interface. In *Proceedings of the 23rd Annual International Conference on Mobile Computing and Networking*, pages 261–274, 2017.

[35] Swadhin Pradhan and Lili Qiu. Rtsense: passive rfid based temperature sensing. In *ACM SenSys*, pages 42–55, 2020.

[36] Vamsi Talla, Joshua Smith, and Shyamnath Gollakota. Advances and open problems in backscatter networking. *GetMobile: Mobile Computing and Communications*, 24(4):32–38, 2021.

[37] R. Tanabe and A. Fukunaga. Success-history based parameter adaptation for differential evolution. In *IEEE Evolutionary Computation (CEC)*, 2013.

[38] G C Topp, J L Davis, and A P Annan. Electromagnetic determination of soil water content : Measurements in coaxial transmission lines. *Water Resources Research*, 16(3):574–582, 1980.

[39] Ju Wang, Omid Abari, and Srinivasan Keshav. Challenge: Rfid hacking for fun and profit. In *MOBICOM*, pages 461–470, 2018.

[40] Ju Wang, Liqiong Chang, Omid Abari, and Srinivasan Keshav. Are rfid sensing systems ready for the real world? In *MobiSys*, pages 366–377, 2019.

[41] Ju Wang, Liqiong Chang, Shourya Aggarwal, Omid Abari, and S. Keshav. Soil moisture sensing with commodity rfid systems. In *MobiSys*, 2020.

[42] Ju Wang, Hongbo Jiang, Jie Xiong, Kyle Jamieson, Xiaojiang Chen, Dingyi Fang, and Binbin Xie. Lifs: low human-effort, device-free localization with fine-grained subcarrier information. In *MOBICOM*, pages 243–256, 2016.

[43] Ju Wang, Jianyan Li, Mohammad Hossein Mazaheri, Keiko Katsuragawa, Daniel Vogel, and Omid Abari. Sensing finger input using an rfid transmission line. In *Sensys*, pages 531–543, 2020.

[44] Ju Wang, Jie Xiong, Xiaojiang Chen, Hongbo Jiang, Rajesh Krishna Balan, and Dingyi Fang. Tagscan: Simultaneous target imaging and material identification with commodity rfid devices. In *MOBICOM*, pages 288–300, 2017.

[45] Liu Wei-Na and Wei Jun-Hong. Effective permittivity of alcohol+ water mixtures as influenced by concentration. *J. Chem. Pharm. Res*, 6:1432–1434, 2014.

[46] Benjamin Daniel Wiltshire, Telnaz Zarifi, and Mohammad Hossein Zarifi. Passive split ring resonator tag configuration for rfid-based wireless permittivity sensing. *IEEE Sensors Journal*, 20(4):1904–1911, 2019.

[47] Bian Wu, Bin Li, Tao Su, and Chang-Hong Liang. Study on transmission characteristic of split-ring resonator defected ground structure. *PIERS online*, 2(6):710–714, 2006.

[48] Jeffries. Wyman. The dielectric constant of mixtures of ethyl alcohol and water from -5° to 40°. *Journal of the American Chemical Society*, 53(9):3292–3301, 1931.

[49] Binbin Xie, Jie Xiong, Xiaojiang Chen, Eugene Chai, Liyao Li, Zhanyong Tang, and Dingyi Fang. Tagtag: material sensing with commodity rfid. In *Sensys*, pages 338–350, 2019.

[50] Diana Zhang, Jingxian Wang, Junsu Jang, Junbo Zhang, and Swarun Kumar. On the feasibility of wi-fi based material sensing. In *MOBICOM*, pages 1–16, 2019.

[51] Pengyu Zhang, Dinesh Bharadia, Kiran Joshi, and Sachin Katti. Hitchhike: Practical backscatter using commodity wifi. In *Sensys*, pages 259–271, 2016.

[52] Pengyu Zhang and Deepak Ganesan. Enabling bit-by-bit backscatter communication in severe energy harvesting environments. In *NSDI*, pages 345–357, 2014.